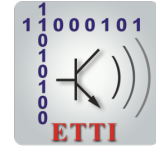




# POLITEHNICA UNIVERSITY OF BUCHAREST



**Doctoral School of Electronics, Telecommunications  
and Information Technology**

Decision No. 938 from 21-10-2022

## **Ph.D. THESIS SUMMARY**

**Eng. Adrian FOCȘA**

---

**METODE AVANSATE DE IMAGISTICĂ RADAR CU APERTURĂ  
SINTETICĂ PENTRU CONFIGURAȚII MONOSTATICE ȘI  
BISTATICE**

**ADVANCED SYNTHETIC APERTURE RADAR COMPUTATIONAL  
IMAGING METHODS FOR MONOSTATIC AND BISTATIC  
CONFIGURATIONS**

---

### **THESIS COMMITTEE**

<b>Prof. Eng. Ion MARGHESCU</b> Politehnica Univ. of Bucharest	President
<b>Prof. Eng. Mihai DATCU</b> German Aerospace Center	PhD Supervisor
<b>Prof. Eng. Tudor-Petru PALADE</b> Technical Univ. of Cluj-Napoca	Referee
<b>Prof. Eng. Andrei ANGHEL</b> Politehnica Univ. of Bucharest	Referee
<b>Assoc. Prof. Eng. Paco DEKKER LOPEZ</b> Delft University of Technology	Referee
<b>Assoc. Prof. Eng. Stefan-Adrian TOMA</b> Military Technical Academy "Ferdinand I"	Referee

**BUCHAREST 2022**

---

# Table of contents

<b>1</b>	<b>Introduction</b>	<b>1</b>
1.1	Presentation of the field of the doctoral thesis . . . . .	1
1.2	Scope of the doctoral thesis . . . . .	1
1.3	Content of the doctoral thesis . . . . .	1
<b>2</b>	<b>Theoretical preliminaries</b>	<b>2</b>
2.1	SAR geometry and spatial resolution . . . . .	2
2.2	SAR signal model . . . . .	3
2.2.1	Classic SAR processors brief review . . . . .	3
2.3	Compressive Sensing . . . . .	3
2.3.1	CS theoretical frame . . . . .	3
2.3.2	CS solvers overview . . . . .	3
2.3.3	Compressive Sensing SAR focusing . . . . .	4
2.4	SAR image enhancement . . . . .	4
<b>3</b>	<b>Sparsity-driven CS-BP-2D SAR processor on ground grid</b>	<b>5</b>
3.1	Introduction to CS-based SAR processors . . . . .	5
3.2	Back-projection algorithm . . . . .	5
3.3	Compressive-sensing key-points . . . . .	6
3.4	CS-BP-2D framework . . . . .	6
3.4.1	Sparsifying dictionary design . . . . .	6
3.4.2	CS recovery aspects . . . . .	6
3.5	Experiments and validation . . . . .	7
3.5.1	Simulated data . . . . .	7
3.5.2	Real-world data . . . . .	7
3.6	Conclusion . . . . .	8
<b>4</b>	<b>CS-based multi-aperture bistatic SAR processor</b>	<b>9</b>
4.1	Bistatic SAR with stationary opportunistic receiver . . . . .	9
4.2	Signal model . . . . .	9
4.2.1	Keystone Transform based RCMC . . . . .	10
4.2.2	Azimuth re-ramping . . . . .	10
4.3	Compressive-sensing reconstruction . . . . .	10
4.3.1	Proposed sparsifying dictionary . . . . .	10

4.4	Multi-aperture exploration . . . . .	10
4.4.1	Auto-regressive model . . . . .	10
4.4.2	CS-FFT . . . . .	10
4.4.3	Proposed processing: CS-CHIRP . . . . .	10
4.5	Experiments and validation . . . . .	11
4.5.1	Empirical imaging scene extent . . . . .	11
4.5.2	Simulated bistatic data . . . . .	11
4.5.3	Real world bistatic data . . . . .	11
4.6	Conclusions . . . . .	13
<b>5</b>	<b>Mode-free Factorized Backprojection SAR processor on ground geometry</b>	<b>14</b>
5.1	Towards Factorized BP solution . . . . .	14
5.2	BP Speed-up . . . . .	14
5.2.1	Sub-aperture factorization . . . . .	14
5.2.2	Polar / elliptical planar grid generation . . . . .	15
5.3	Scan-aware FBP-based SAR imaging . . . . .	16
5.4	Real world validation . . . . .	17
5.4.1	Monostatic raw data . . . . .	17
5.4.2	Bistatic acquisition . . . . .	18
5.4.3	Results . . . . .	18
5.5	Conclusion . . . . .	19
<b>6</b>	<b>TOPSAR denoising</b>	<b>20</b>
6.1	Problem description and current solutions . . . . .	20
6.2	Proposed workflow . . . . .	20
6.2.1	Gaussian Process Regression . . . . .	21
6.2.2	Incidence angle compensation . . . . .	21
6.3	Results . . . . .	21
6.4	Conclusions . . . . .	21
<b>7</b>	<b>Conclusions</b>	<b>23</b>
7.2	Original contributions . . . . .	23
7.3	List of original publications . . . . .	24
	<b>References</b>	<b>25</b>

# Chapter 1

## Introduction

### 1.1 Presentation of the field of the doctoral thesis

Most of the ended or ongoing Synthetic Aperture Radar (SAR) missions are using adapted SAR processors, harnessing the particularities of the acquisition setup. Recent studies reveal the time-domain SAR processors [26] are the most appropriate for future innovative SAR missions [6, 16], due to their straightforward accommodation concerning the scanning scenario and the possibility of integrating quality enhancing modules (e.g., motion compensation, auto-focus).

### 1.2 Scope of the doctoral thesis

The thesis aims to design efficient SAR imaging solutions concerning both SAR image formation and SAR image enhancement.

### 1.3 Content of the doctoral thesis

Chapter 2 presents the theoretic preliminaries. Chapter 3 presents a focusing solution involving fewer data than the classic SAR processors and simultaneously making use of the back-projection algorithm versatility. Chapter 4 introduces a focusing workflow suited for the bistatic context created by a space-borne transmitter working on TOPSAR mode and a stationary ground-based receiver which captures intermittent data from more than one transmitter apertures. Chapter 5 presents a time domain SAR processor in conjunction with an appropriate elliptical grid and a special angular restricted back-projection operation. Chapter 6 introduces a novel approach for denoising the cross polarization detected SAR images recorded on TOPSAR mode.

# Chapter 2

## Theoretical preliminaries

### 2.1 SAR geometry and spatial resolution

The platform containing the transmitter ( $T_x$ ) and the receiver ( $R_x$ ) depicted in Fig. 2.1, travels along a rectilinear trajectory while periodically (PRI - pulse repetition interval) emitting pulses and receiving electromagnetic reflections back from the illuminated scene.

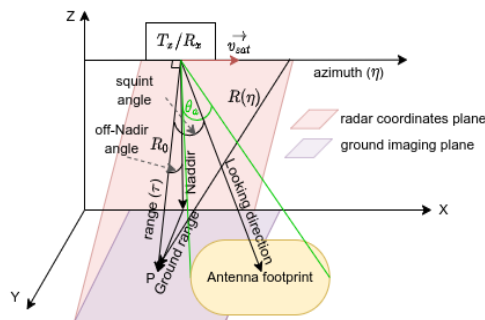


Fig. 2.1 Simplified monostatic SAR geometry

The main geometric aspects of a monostatic acquisition are displayed in Fig. 2.1. The azimuth direction is parallel to the platform velocity and together with the range direction form the radar (two-dimensional) coordinates. By varying the squint angle and the off-Nadir angle many monostatic scan modes may be obtained (STRIPMAP, TOPSAR, SCANSAR, SPOTLIGHT). The range resolution is inversely proportional to the transmitted signal bandwidth whereas the azimuth resolution is directly linked to the dwell time.

## 2.2 SAR signal model

### 2.2.1 Classic SAR processors brief review

The ideal SAR image formation is achieved by the Matched Filter (MF), However, it is the most computational demanding since it needs space variant coefficients. The frequency domain algorithms such as Range-Doppler, Chirp-Scaling and w-K perform the SAR image formation faster than MF but they typically use approximations to accommodate a specific acquisition setups. Moreover, they are not able to process azimuth folded spectrum as is the case of TOPSAR mode.

## 2.3 Compressive Sensing

### 2.3.1 CS theoretical frame

The theory of compressive sensing (CS) [7] guarantees the perfect reconstruction of the original signal  $\mathbf{x}$  from less samples than the lower bound established by the Nyquist sampling theorem. The classic model of CS is depicted by (2.26). In (2.26),  $\Phi \in \mathbb{C}^{p \times n}$  denotes the measurement matrix,  $\Psi \in \mathbb{C}^{n \times n}$  is the over-complete sparsifying basis,  $x \in \mathbb{C}^n$  and  $y \in \mathbb{C}^p$  represents the original signal and the available samples, with  $p < n$  whereas  $\varepsilon \in \mathbb{C}^p$  is a vector modeling the noise.

$$y = \Phi\Psi\alpha + \varepsilon = \Theta\alpha + \varepsilon \quad (2.26)$$

The sparse representation of  $x$  is depicted in (2.27).

$$\mathbf{x} = \Psi\alpha, \|\alpha\|_0 = K \quad (2.27)$$

In (2.27),  $K$  denotes the sparsity degree and formally is depicted by  $L_0$  norm (cardinality of non-null coordinates sub-set of  $\alpha$ ). The problem of recovering  $x$  starts with solving (2.28) and then replacing the outcome into equation (2.27).

$$\min_{\alpha} \|y - \Theta\alpha\|_2^2 \quad s.t. \quad \|\alpha\|_0 = K \quad (2.28)$$

### 2.3.2 CS solvers overview

In principle the CS solvers may be grouped in three categories: greedy solvers (e.g., Orthogonal Matching Pursuit (OMP), Regularized OMP, Generalized OMP), convex relaxed solvers that typically use  $L_1$  norm instead of  $L_0$  norm (e.g., SPGL1-BPDN) and non-convex solvers (e.g., Iterative Jumping Thresholding, Bayesian CS) that either use sub-unitary norms or put the CS problem in terms of Bayesian framework.

### **2.3.3 Compressive Sensing SAR focusing**

When posing the SAR focusing problem in terms of CS, one should account for the following aspects: identifying the sparsity domain, choosing the appropriate under-sampling method and applying a suitable CS solver. The state-of-the-art solutions chose a classic SAR processor and adapt its steps to CS workflow.

## **2.4 SAR image enhancement**

Apart from the well-known pixel-value to radar cross section radiometric calibration/conversion, a particular radiometric problem, recently reported in the scientific literature, is the one that may occur when using TOPSAR scanning modes on low back-scattering areas (calm water, desert). The effect arises especially on the cross-polarization SAR images and therefore, a denoising procedure should be applied prior to feeding the SAR image (detected) to the end process applications (classification/regression, parameter inversion). Even though some calibration procedures were developed [28, 18, 20, 4, 19] there is still room for improvements in solving this problem.

# Chapter 3

## Sparsity-driven CS-BP-2D SAR processor on ground grid

### 3.1 Introduction to CS-based SAR processors

This chapter introduces a combined CS-BP SAR imaging framework called CS-BP-2D for a user-defined grid which manages to discard raw data while preserving the magnitude and the phase of the SAR image. It exploits the spatial sparsity propriety characterizing some urban areas and bistatic scenarios. We derive Back-projection basis. Compared to the other CS-based techniques [1], [8] our approach does not need to decouple range and azimuth. Besides, CS-BP-2D has no need for range cell migration correction. The solver chosen for the CS problem is the orthogonal matching pursuit (OMP) reconstruction algorithm [5]. The processing flow also includes a nonlinear filter that reduces the artifacts. It is based on SAR system point spread function (PSF).

### 3.2 Back-projection algorithm

In [17],[27], MATLAB implementations of BP are presented. Basically, BP involves the following linear processing steps:

A1. Apply a matched filter on every received signal (either in the time domain or in the frequency domain), generating the range-compressed signal.

A2. Linearly interpolate every range-compressed signal from step A1 on a pre-defined focusing grid.

A3. Sum up phase-corrected contributions of every range-compressed signal to each grid cell to generate the complex SAR image.

### 3.3 Compressive-sensing key-points

In order to put the BP focusing as a CS problem we have employed random sub-Nyquist sampling matrix, BP linear operator as sparsifying dictionary and OMP as solver. The estimation of the sparsity degree becomes more relaxed (over-estimated) due to the use of the PSF-driven kernel which cleans the CS-raw output.

### 3.4 CS-BP-2D framework

The diagram in Fig. 3.3 illustrates the proposed workflow. Depending on the dimensions of the BP operator i.e., System Transformation Matrix (STM), the CS recovery algorithm may be applied either on patches or for the entire grid at once. For the first case, the modified OMP algorithm outcomes are eventually assembled into the full SAR image.

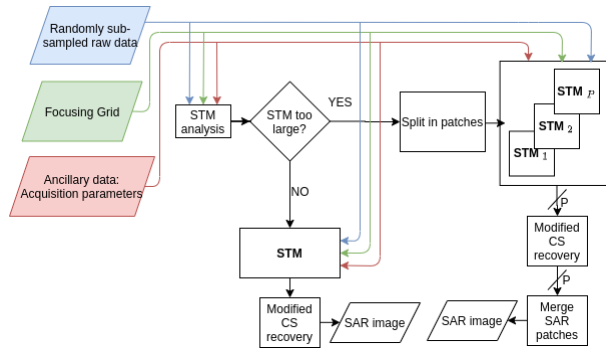


Fig. 3.3 CS-BP-2D workflow

The main contributions of the proposed processing chain are the following: (i) it is independent of the SAR scanning mode, (ii) CS-BP-2D has no need for azimuth range decoupling, (iii) it assures a straightforward accommodation for monostatic and bistatic acquisition scenarios, and (iv) provides a modified CS solver which involves the system's PSF for artifact suppression. Also, the PSF-based filter accounts for the grid mismatch errors. The proposed processing is flexible concerning the input data. CS-BP-2D may be applied directly on range compressed data.

#### 3.4.1 Sparsifying dictionary design

The sparsifying dictionary is constructed according to the BP steps involving the imaging grid, the randomly under-sampled data and the acquisition ancillary data.

#### 3.4.2 CS recovery aspects

Since for the reconstruction we have chosen a greedy CS solver, one important aspect is the estimation of the sparsity degree ( $K$ ). In our case the precision on  $K$  estimate is relaxed by the use of the nonlinear PSF filter.

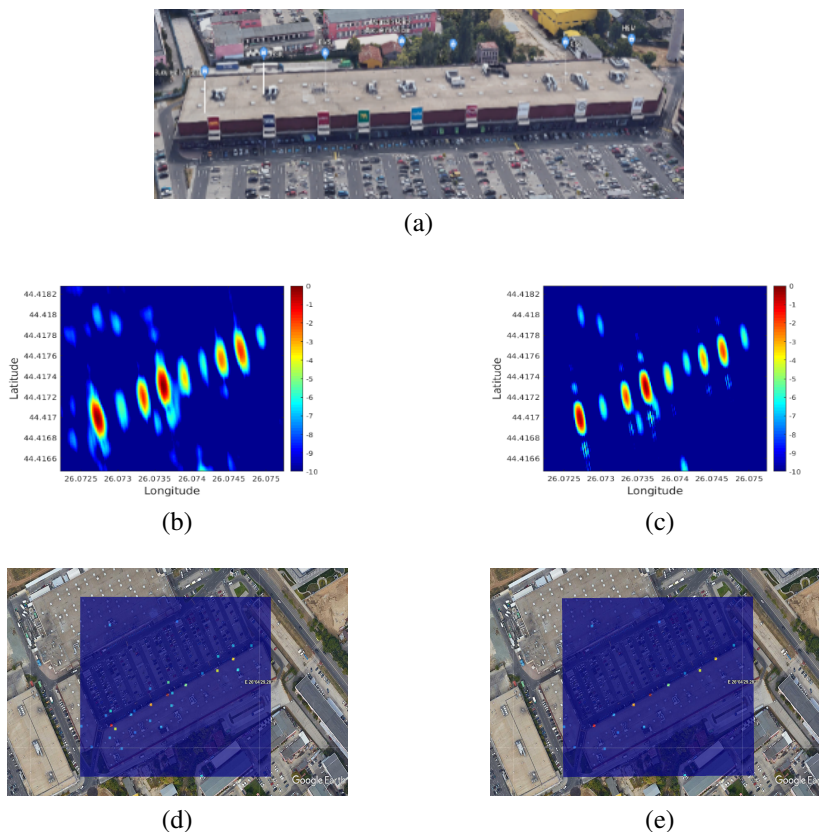


Fig. 3.15 VVC area results: a) Optical image, b) BP outcome [dB], c) CS-BP-2D SAR image (with PSF) [dB], d) CS-BP-2D (without filter) and e) CS-BP-2D (with filter) overlaying Google Earth optical images

## 3.5 Experiments and validation

### 3.5.1 Simulated data

Simulated data was used to prove the effectiveness of the proposed algorithm with respect to magnitude and phase preservation. Additionally, some tests for evaluating the robustness of the CS-BP-2D workflow to the signal-to-noise ratio and to the real sparsity degree were carried out.

### 3.5.2 Real-world data

In the following, for a region of  $200m \times 240m$  containing Vulcan Value Center, Bucharest (VVC), experiments testing the CS-BP-2D were conducted. The chosen area is representative because it contains point-like targets, and the hypothesis of spatial sparsity holds. The outcome provided by the recovery algorithm consists of isolated reconstructed points, i.e., a superposition of Delta functions, e.g. Fig. 3.15d – raw result obtained by CS-BP (without filter) and Fig. 3.15e-CS-BP-2D. For a better visualization, these results are convoluted with a modified system PSF,[9] e.g. Fig. 3.15c.

As displayed in Fig. 3.15, after the PSF-based filter is applied, the remaining points match the logo panels locations.

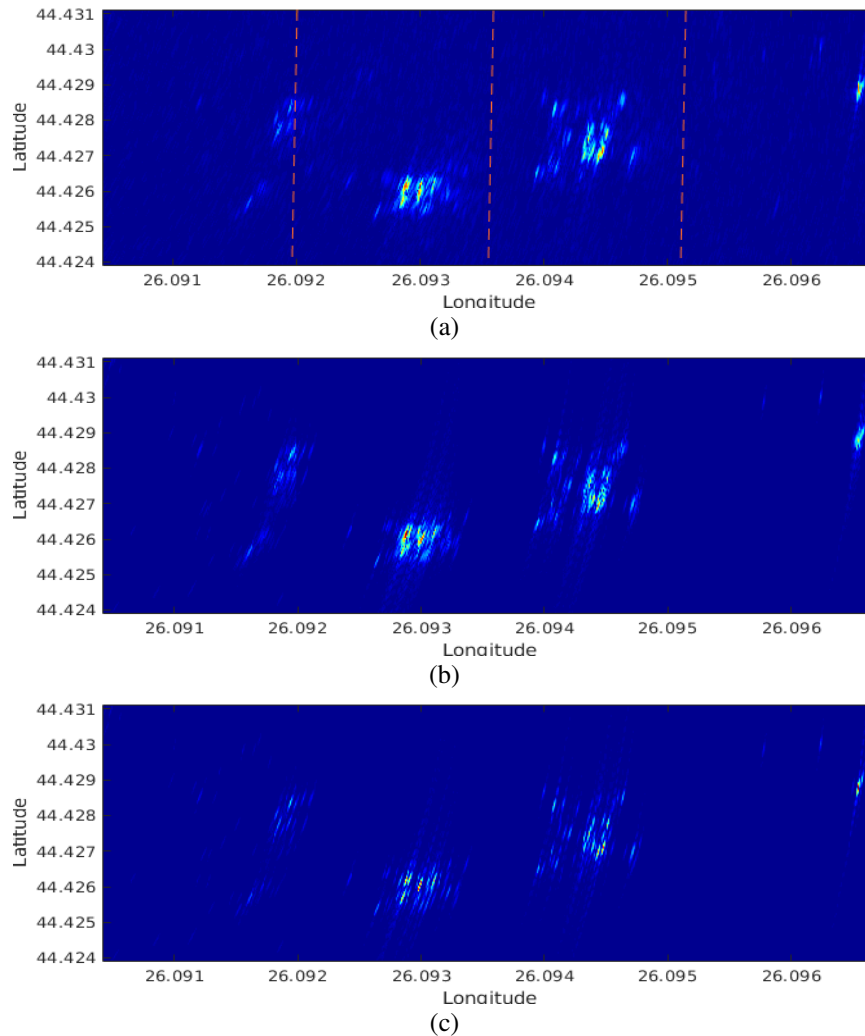


Fig. 3.20 Imaging results on bistatic real-world data. a) BP SAR image, b) CS-BP (without filter) SAR image, c) CS-BP-2D SAR image

The evaluation was assessed also for a bistatic configuration formed by Sentinel-1 transmitter and COBIS [2] receiver. The comparative results are displayed in Fig. 3.20.

### 3.6 Conclusion

In this chapter, a Back-Projection – Compressed Sensing SAR focusing algorithm (for a user-defined grid) was proposed. Both benefits inherited from BP and Matching Pursuit are exploited. The BP sparsifying basis was designed together with a PSF-based artifact rejection filter. The obtained SAR images are focused on geo-referenced grids having, in principle, no need for coregistration in future interferometric applications.

# Chapter 4

## CS-based multi-aperture bistatic SAR processor

This chapter introduces a compressive sensing (CS)-based approach for increasing bistatic synthetic aperture radar imaging quality in the context of a multi-aperture acquisition. The proposed processing scheme exploits the natural sparsity characterizing the illuminated scene. The sparse data from multiple apertures are available as a result of TOPSAR scanning mode. The multi-aperture data may come from both Tx side-lobes and side-sections in the main lobe when the Tx antenna is oriented to the other two sub-swaths.

### 4.1 Bistatic SAR with stationary opportunistic receiver

The sparse data from multiple apertures are available as a result of TOPSAR scanning mode. The multi-aperture data may come from both Tx side-lobes and side-sections in the main lobe when the Tx antenna is oriented to the other two sub-swaths.

### 4.2 Signal model

The stationary receiver (COBIS) has one channel looking towards Sentinel-1 transmitter (synchronization channel) and at least one channel oriented towards the scene of interest. Since the signal in the sync channel is used for the range matched filtering, the azimuth bandwidth of the range compressed data become very narrow and also the footprint of a point target experiences a linear coupling between range and azimuth.

### **4.2.1 Keystone Transform based RCMC**

The proposed processing which involves azimuth profiles reconstruction first decouples range and azimuth via a Keystone Transform thus achieving the Range Cell Migration Correction.

### **4.2.2 Azimuth re-ramping**

Another important asset of the method is that it uses a chirp-based sparsifying dictionary. Therefore, prior to the reconstruction, the semi-monostatic hyperbolic variation is restored which is called azimuth re-ramping.

## **4.3 Compressive-sensing reconstruction**

The goal of the method is to recover sub-intervals in the multi-aperture data characterized by low signal to noise ratio under the assumption of spatial sparsity. In this regard we employed various CS solvers.

### **4.3.1 Proposed sparsifying dictionary**

The sparsifying dictionary  $\Psi$  is formed using an average chirp-like (hyperbolic phase) response obtained from a mid-scene point target (reference signal). Each dictionary atom is a time-shifted version of the reference chirp signal.

## **4.4 Multi-aperture exploration**

### **4.4.1 Auto-regressive model**

A commonly used tool for reconstructing one-dimensional data containing gaps is the auto-regressive (AR) model. However, it works properly on small gaps.

### **4.4.2 CS-FFT**

A direct implication of the narrow azimuth bandwidth obtained after the range compression is that the profile reconstruction may employ the Fourier basis as sparsity dictionary. Nevertheless, the approximation does not ensure a proper recovery of the signal.

### **4.4.3 Proposed processing: CS-CHIRP**

The proposed bistatic SAR focusing procedure is depicted in Fig. 4.5. Before applying the conventional BP, the azimuth profiles are recovered via CS framework.

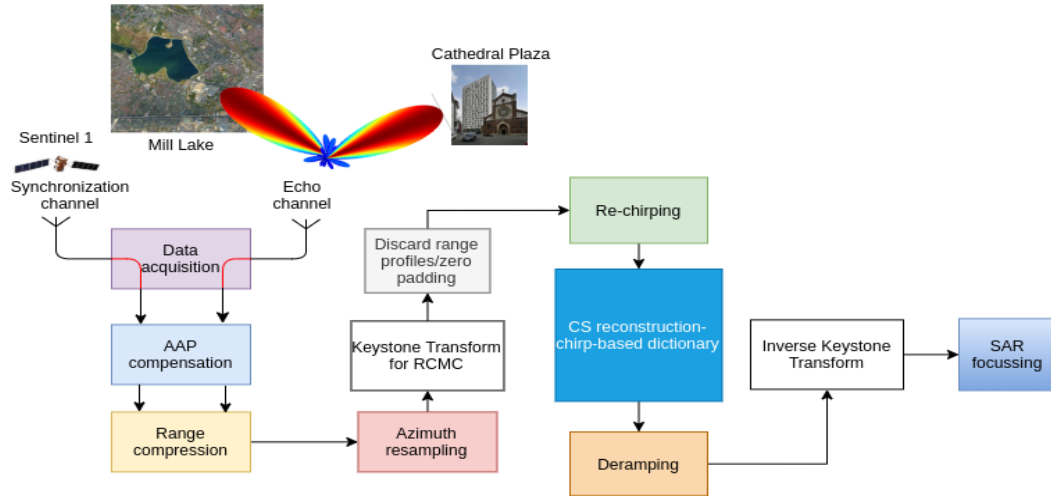


Fig. 4.5 Sparse multi-aperture reconstruction framework: CS-CHIRP

## 4.5 Experiments and validation

### 4.5.1 Empirical imaging scene extent

The simulated data proves that the mid-scene point used to form the chirp-based dictionary ensures a reasonable recovery.

### 4.5.2 Simulated bistatic data

Since there is no ground truth for multi-aperture data, we have used simulated bistatic data to provide a qualitative evaluation over different CS solvers.

### 4.5.3 Real world bistatic data

Concerning the real-world data, two study cases were analyzed. The first one is a particular case in which the receiver looking direction and the transmitter-receiver segment projected on the ground imaging plane are co-linear. The second one is a more general case.

The bistatic SAR images in Fig. 4.10 illustrate an urban area of  $950 \text{ m} \times 2350 \text{ m}$  from Bucharest, Romania. In Fig. 4.10a the focused SAR image is obtained from a single aperture interval ( $0.323\text{s}$ ). The raw integration of the multi-aperture interval ( $1.7905\text{s}$ ) is shown in Fig. 4.10b. The SAR images resulted after reconstruction of the azimuth profiles are presented in Fig. 4.10c - Fig. 4.10i. All methods manage to reduce the effect of the grating lobes. Yet some important observations should be highlighted: CS-FFT methods fail (strong scatterers' main lobes are smeared in the azimuth direction) even though it seems to generate a "clean" SAR image. Generally, the CS-CHIRP methods outperform CS-FFT and AR reconstructions.

# Advanced Synthetic Aperture Radar Computational Imaging Methods for Monostatic and Bistatic configurations

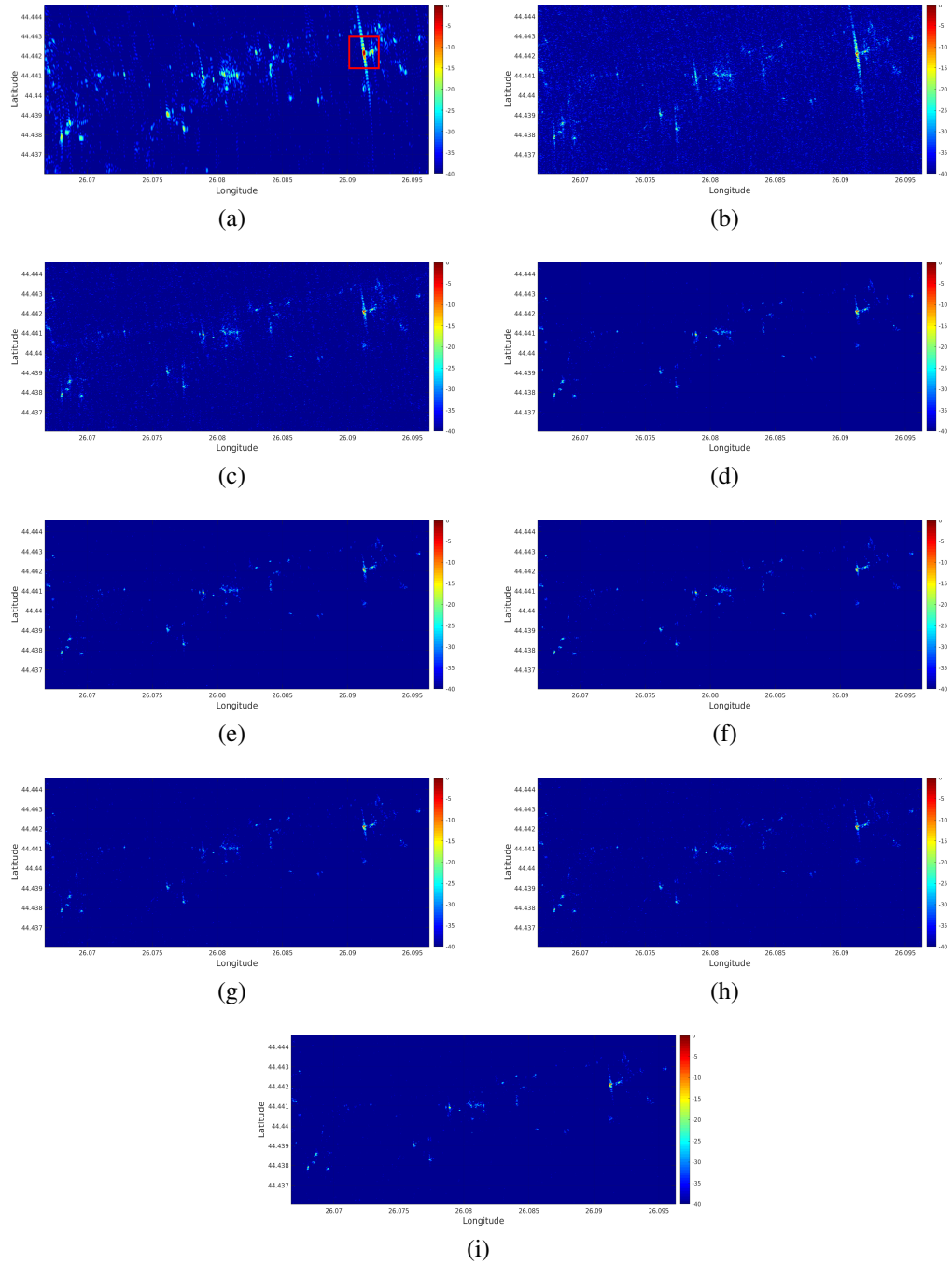


Fig. 4.10 Extended scene imaging results: a) Single aperture, b) Multi-aperture raw integration, c) AR, d) GOMP- $\Psi^{CHIRP}$ , e) CoSaMP- $\Psi^{CHIRP}$ , f) SWAP- $\Psi^{CHIRP}$ , g) IJT- $L_{2/3}$ - $\Psi^{CHIRP}$ , h) SPGL1-BPDN- $\Psi^{CHIRP}$ , and i) FISTA- $\Psi^{FFT}$

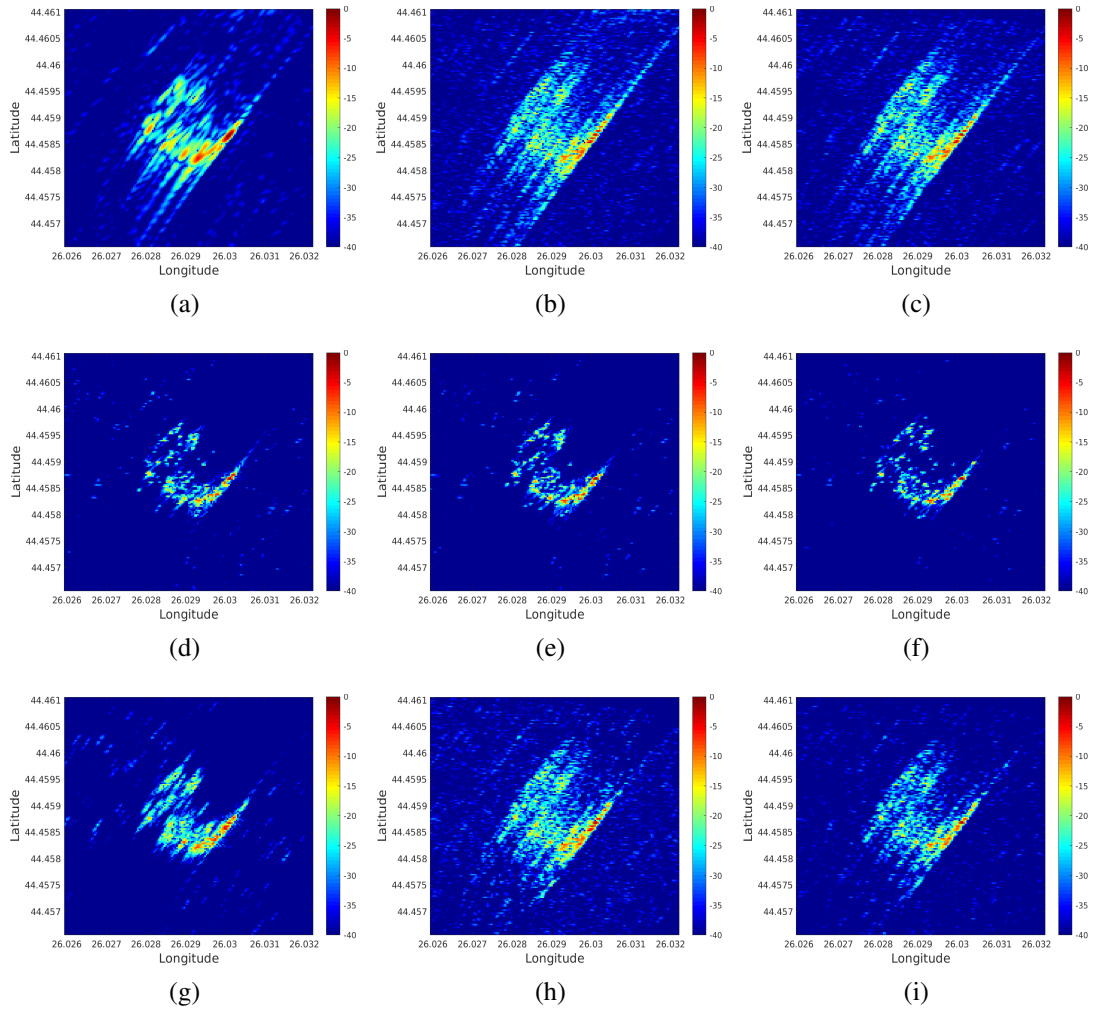


Fig. 4.20 Normalized bistatic SAR images (in dB [-40, 0]) over Mill Lake Peninsula (green frame): a) single aperture b) raw data integration c) AR d) CoSaMP- $\Psi^{CHIRP}$ , e) GOMP- $\Psi^{CHIRP}$ , f) CMP- $\Psi^{CHIRP}$ , g) GOMP- $\Psi^{FFT}$ , h) IJT- $L_{2/3}$ - $\Psi^{CHIRP}$ , i) SPGL1-BPDN- $\Psi^{CHIRP}$

The second image (general study case) covers a  $500\text{m} \times 500\text{m}$  area and is centered on [44.45881 N, 26.02909 E]. Without azimuth reconstruction, the side-lobes corresponding to the scatterers from the Mill Lake peninsula cover a significant part of the water-body.

## 4.6 Conclusions

The chapter presented a CS-based methodology for resolution enhancement in the context of an opportunistic bistatic SAR imaging having Sentinel-1 as a transmitter and COBIS as a ground-based receiver. The use of the CS concept for signal reconstruction is essentially based on spatial sparsity assumption on each iso-range and the use of a chirp-based sparsifying dictionary.

# Chapter 5

## Mode-free Factorized Backprojection SAR processor on ground geometry

### 5.1 Towards Factorized BP solution

Even though the computational burden of the classic BP is less than the one corresponding to the matched filter ( $\mathcal{O}(n^4)$ ), many efforts were devoted to accelerating the BP implementation. Fast implementations of BP, firstly introduced in [30]  $\mathcal{O}(n^{2.5})$  and [29], were recently approached in many works.

### 5.2 BP Speed-up

Factorized Back-projection [29] stands on the idea of appropriately generating the focusing grid such that the sampling requirements, typically on the cross-range direction become more relaxed. Specifically, for the monostatic case, a polar grid has to be employed whereas the bistatic configurations need ellipsoidal grids.

#### 5.2.1 Sub-aperture factorization

As depicted in [30], the BP SAR image may be obtained as a coherent summation of independent sub-aperture images (5.3).

$$I_{BP}(P) = \sum_{l=1}^L \int_{-\frac{T}{2}+(l-1)\Delta T}^{-\frac{T}{2}+l\Delta T} s_{rc}(\Delta R_P, \eta) \cdot \exp(jk_r \Delta R_P) d\eta \quad (5.3)$$

Also, in [30], for each sub-aperture a different polar grid is formed prior to interpolate it to the fine Cartesian grid.

### 5.2.2 Polar / elliptical planar grid generation

In the following, a general (bistatic) vectorial procedure for polar / elliptical grid generation on arbitrary planes (e.g., ground grid) is introduced. We propose a grid generation routine for arbitrary plane that determines the 3D coordinates of the points laying on ellipse arcs for FBP-based SAR processors.

The grid points are determined in a two-step procedure. First, the grid generation origin ( $\vec{r}_C$ ) is computed. Then, the second stage consists in determining the grid points solving a constraint ellipsoid equation. The first stage is important since it produces a unique solution for the second stage. Fig. 5.3 illustrates the geometric elements involved in the computations of  $\vec{r}_C$  whereas Fig. 5.4 highlights the derivation of an arbitrary point  $\mathbf{P}$  having  $(\Delta R_P, \theta)$  as elliptical coordinates.

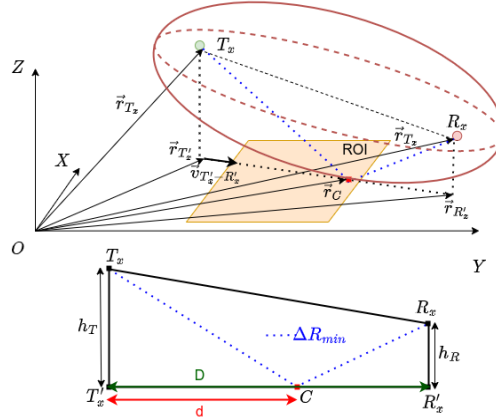


Fig. 5.3 Geometric elements for determination of the local elliptical center ( $\vec{r}_C$ ) in the plane containing the ROI

As the bistatic iso-range surface is a rotational ellipsoid, computing the grid generation origin  $\vec{r}_C$  may simplify to the problem suggested by the trapeze in the bottom part of Fig. 5.3. Hence,  $\vec{r}_C$  is computed via (5.4) and represents the intersection of the minimum iso-range ellipsoid ( $\Delta R_{min}$ ) and the plane containing the ROI. In (5.4),  $\vec{v}_{T'_x-R'_x}$  is a unit vector having the origin in the transmitter projection onto the ROI plane ( $\vec{r}_{T'_x}$ ) and the orientation towards the receiver projection ( $\vec{r}_{R'_x}$ ) onto the ROI plane.

$$\vec{r}_C = \vec{r}_{T'_x} + d\vec{v}_{T'_x-R'_x} \quad (5.4)$$

The coefficient  $d$  in (5.4) is determined using (5.5).

$$d = \operatorname{argmin} \{ \Delta R(d) \} \quad (5.5)$$

The explicit form for  $\Delta R(d)$  together with the list of constraints are highlighted in the trapeze  $T_x T'_x R'_x R_x$  in Fig. 5.3.

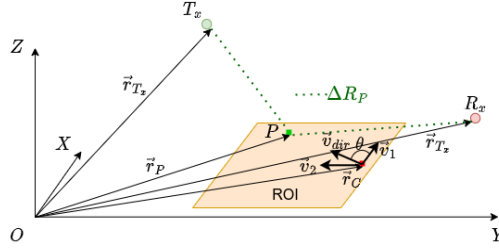


Fig. 5.4 Geometric elements for the determination of the position of a point  $\mathbf{P}$  laying in the  $\vec{v}_{dir}$  direction on the intersection between the ellipsoidal iso-range  $\Delta R_P$  and the ROI

Once the elliptical center  $\vec{r}_C$  has been determined, the grid points location  $\vec{r}_P$  may be computed using (5.8).

$$\vec{r}_P = \vec{r}_C + \gamma \vec{v}_{dir} \quad (5.8)$$

In (5.8),  $\vec{v}_{dir}$  represents a unit vector suggesting the angular partitioning of the grid that may be computed via (5.9) using some arbitrary orthonormal vectors  $\vec{v}_1$  and  $\vec{v}_2$  in the plane containing the ROI.

$$\vec{v}_{dir} = \vec{v}_1 \cos(\theta) + \vec{v}_2 \sin(\theta) \quad (5.9)$$

For a fixed iso-range  $\Delta R$  and a chosen direction  $\vec{v}_{dir}$ ,  $\gamma$  is found by solving (5.10) by replacing  $\vec{r}_P$  from (5.8).

$$\|\vec{r}_P - \vec{r}_{Tx}\| + \|\vec{r}_P - \vec{r}_{Rx}\| = \Delta R \quad (5.10)$$

### 5.3 Scan-aware FBP-based SAR imaging

The proposed processor works as follows. Firstly, the P/E (coarse and fine) grid is created. Then, the entire aperture is split into  $L$  sub-apertures (SA) and the coarse resolution SAR images are obtained using the backprojection operation on the UFR-free (Unfolding and Resampling) range compressed profiles. Normally, the backprojection of the range compressed signal onto the focusing grid is performed only by considering a "range rule" (the backprojection area is an annulus) consisting in finding each pixel value via an interpolation kernel. However, this single condition would not satisfy the azimuth ambiguity-free region ensured by the pulse repetition frequency (PRF). Hence, the SAR processor should accommodate this problem through special processing. For example, in the current Sentinel-1 Level-1 (L1) processor for TOPS mode, the raw data is aliased in the azimuth direction, thus an UFR step is performed before applying the azimuth compression. An important feature of the proposed processor which makes it cope with various scan modes is that the backprojection step is performed in an angle restricted area. Afterward, all sub-aperture (coarse-resolution) SAR images are interpolated to the fine P/E ground grid and coherently added to form the fine P/E grid SAR image (SLC image).

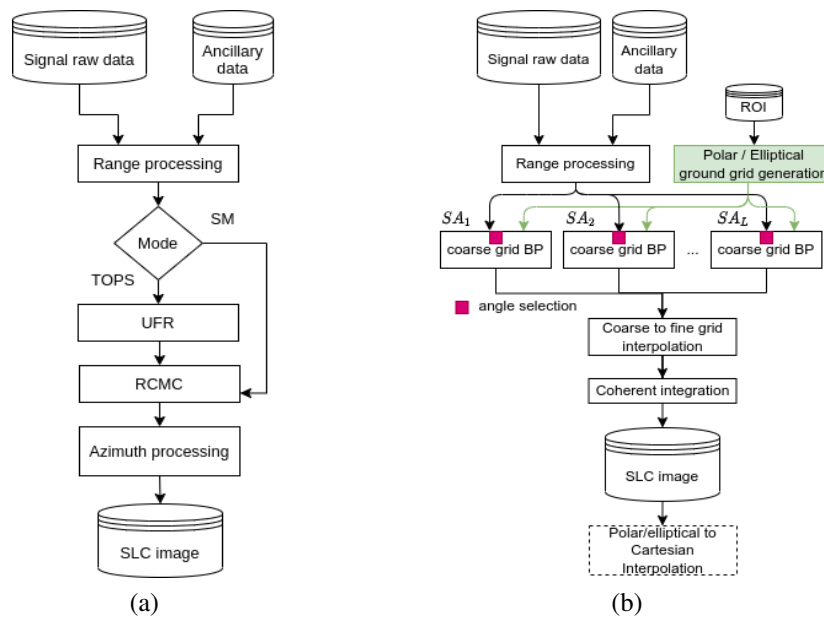


Fig. 5.7 SAR processors: a) Simplified Sentinel-1 operational RDA [23] and, b) proposed FBP-based processor with pixel selection block (magenta square) accommodating beam-sweeping SAR scan modes and both monostatic and bistatic configurations through P/E ground grid generation block

## 5.4 Real world validation

### 5.4.1 Monostatic raw data

The performance comparison regarding the impulse response function (IRF) parameters is determined only on IW-mode. A real-world IRF located at [52.252830 N, 4.11069 E] obtained using an European Space Research and Technology Centre (ESTEC) transponder located at west Noordwijk, Netherlands is evaluated.

Table 5.1 PERFORMANCE PARAMETERS COMPARISON OF THE IRF IN THE MONOSTATIC CASE

		PSLR [dB]	ISLR [dB]	$\delta_{-3dB}$ [m]
L1-product ideal IRF	range	>21.2	<-16.1	3.10
	azimuth	>21.2	<-16.1	22.7
L1 product real IRF	range	20.70	-16.40	3.07
	azimuth	20.90	-16.68	22.83
proposed real IRF	range	19.99	-16.56	3.10
	azimuth	20.17	-16.94	22.80

The following quality parameters were considered: the peak to side-lobe ratio (PSLR), the integrated to side-lobe ratio (ISLR), and the resolution computed at -3dB ( $\delta_{-3dB}$ ). The obtained product parameters are compliant to [21].

## 5.4.2 Bistatic acquisition

The acquisition scenario was formed by Sentinel-1 transmitter and COBIS ground based receiver.

## 5.4.3 Results

### Monostatic

The evaluation on SM mode (S6) is performed by focusing the SAR data containing Fogo island, Cape Verde. The SAR image extents displayed in Fig. 5.9a are  $30 \text{ km} \times 30 \text{ km}$ . The two TOPS-mode examples in the Sentinel-1 scanning configurations are also verified for a region containing Bucharest, Romania (IW) and Sisimiut, Greenland (EW).

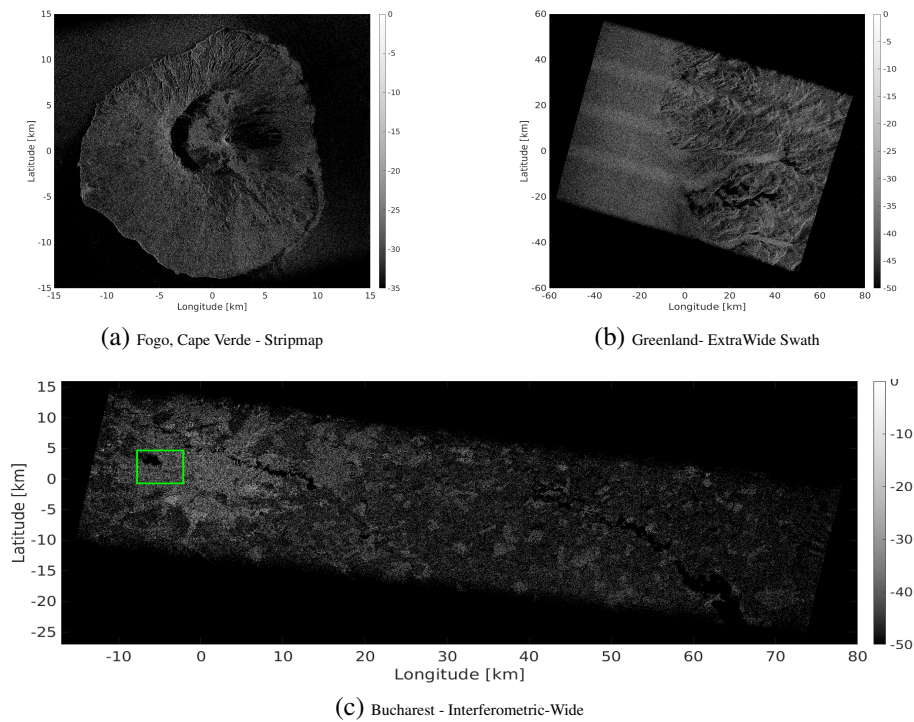


Fig. 5.9 Monostatic SAR imaging results (magnitude component in dB) obtained from UFR-free data

The proposed processor imaging results for TOPSAR modes are shown in Fig. 5.9c and, Fig. 5.9b respectively. The two acquisitions were performed on the 3<sup>rd</sup> of March 2020 for IW and on the 12<sup>th</sup> of April 2021 for the EW mode.

### Bistatic

The proposed SAR image formation procedure which harnesses the angular pixels selection and an adapted ground-fixed grid generation is compared to the conventional

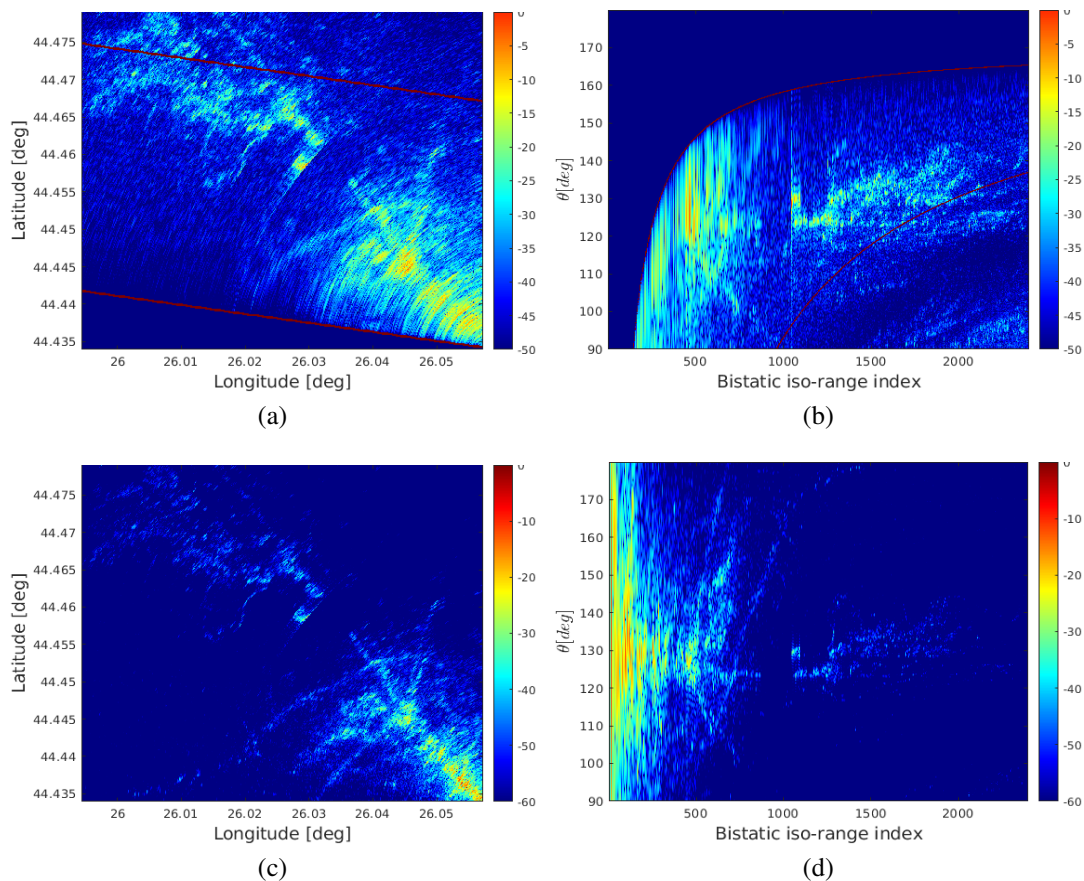


Fig. 5.14 Bistatic SAR images magnitude in dB for the first sub-experiment: a) Intermediate step in pixel-by-pixel update BP for Sentinel-1 descending orbit, b) intermediate result in bistatic FBP on uniformly sampled ground plane elliptical coordinates, c) final bistatic SAR image represented in uniformly sampled ground plane elliptical coordinates, and d) bistatic SAR image displayed in uniformly sampled ground Cartesian coordinates

BP applied on a uniformly spaced ground grid in Fig. 5.14. The pixel selection step, using the Sentinel-1 antenna ground footprint is highlighted in Fig. 5.14a for the uniformly spaced Cartesian grid. The elliptical coordinate correspondent of Fig. 5.14a is displayed in Fig. 5.14b. The area between the red curves in Fig. 5.14a and Fig. 5.14b contains the pixels updated through the backprojection of the very last range profile processed. The final SAR image obtained in P/E coordinates, Fig. 5.14d is finally interpolated to the Geo-coded planar grid (uniformly spaced) forming the output shown in Fig. 5.14c. The pixel spacing for the Cartesian planar grid [Fig. 5.14c] was 5m in both latitude and longitude directions.

## 5.5 Conclusion

In this chapter, we proposed a mode-free/scenario-free FBP-based SAR focusing framework with special attention on the ground grid generation constrained by the bistatic SAR imaging particularities and the angle-based pixel selection step.

# Chapter 6

## TOPSAR denoising

### 6.1 Problem description and current solutions

ESA Copernicus program comprises Sentinel-1 A/B, a pair of polar orbit satellites equipped with C-band SAR sensors able to map the Earth using 4 scanning modes in either single or dual polarization: STRIPMAP, Interferometric Wide(IW), ExtraWide (EW) and Wave Mode (WV). Among all products, under weak back-scattering conditions (e.g., calm water-bodies, desert) the cross-polarization detected (Ground Range Detected Magnitude (GRDM) products) TOPSAR images i.e., IW and EW are more affected by scalloping in the azimuth direction and by the thermal noise in the range direction. Even though starting with Instrument Processing Facility (IPF) 2.90 both azimuth and range noise vectors are provided in the product ancillary files, the denoising method [24], the obtained results are not always satisfactory.

### 6.2 Proposed workflow

The proposed denoising processing flow is based on the recovery of the data lost after applying [24] with data inferred through Gaussian Process Regression (GPR). First, both co-polarized and cross-polarized GRDM SAR images are corrected using [24]. Then, the incidence angle compensation is applied. Further, using reliable areas (high SNNR defined in [22]) in each the dual-pol SAR images the kernel-based GPR model is trained. The training process learns the physical signature translation from co-polarized data to cross-polarized data. The input data is represented by the ESA denoised - incidence angle corrected cross-polarized pixels whereas the output is the corresponding co-polarized pixels. In the proposed method, the final denoised image is obtained by combining the GPR prediction with the an over-denoised image obtained using [24]. The two components are weighted using a mask. The mask is obtained in a two step process. When the subtraction of the 2D noise field from the noisy image is performed, the negative and null values positions are stored and a new image containing ones on those

positions and zeros otherwise is formed. Then, this binary mask is 'smeared' using a  $7 \times 7$  circular filtering kernel resulting the final weights mask.

### 6.2.1 Gaussian Process Regression

Even though Gaussian Process Regression is a powerful Bayesian prediction tool, it has been presented relatively recently [25] as a Machine Learning technique. GPR was previously known as Kriging interpolation. It has been successfully employed for physical parameters mapping in the context of polarimetric SAR data [3]. In our case GPR is used to map the co-pol data into the cross-pol data.

### 6.2.2 Incidence angle compensation

Since the incidence angle is not included as input data in the GPR, both cross-polarization and co-polarization images are corrected.

## 6.3 Results

In this section the denoised images resulted by applying the proposed denoising workflow are displayed and compared to the ones obtained by [24]. The four denoised example images displayed in Fig. 6.8 correspond to the products (example-1,....,example-4) listed below:

- S1A\_EW\_GRDM\_1SDH\_20210621T072157\_20210621T072257\_038435\_04890F\_A9C0
- S1A\_EW\_GRDM\_1SDH\_20210620T064151\_20210620T064251\_038420\_0488A2\_65A8
- S1B\_EW\_GRDM\_1SDH\_20190124T074426\_20190124T074526\_014633\_01B458\_E8F5
- S1A\_EW\_GRDM\_1SDH\_20210307T070530\_20210307T070630\_036889\_0456BB\_881C

## 6.4 Conclusions

In this chapter we proposed a technique for reducing the thermal noise in Sentinel-1 EW GRDM products recorded over weak back-scattering scenarios. To our knowledge, it is the first denoising procedure to benefit from the co-polarization image. Beside the visual enhancement of the denoised image, the average range profiles (red curves in Fig. 6.8) proves that our method also boosts the inter-swath energy balancing by exploiting the co-polarization channel.

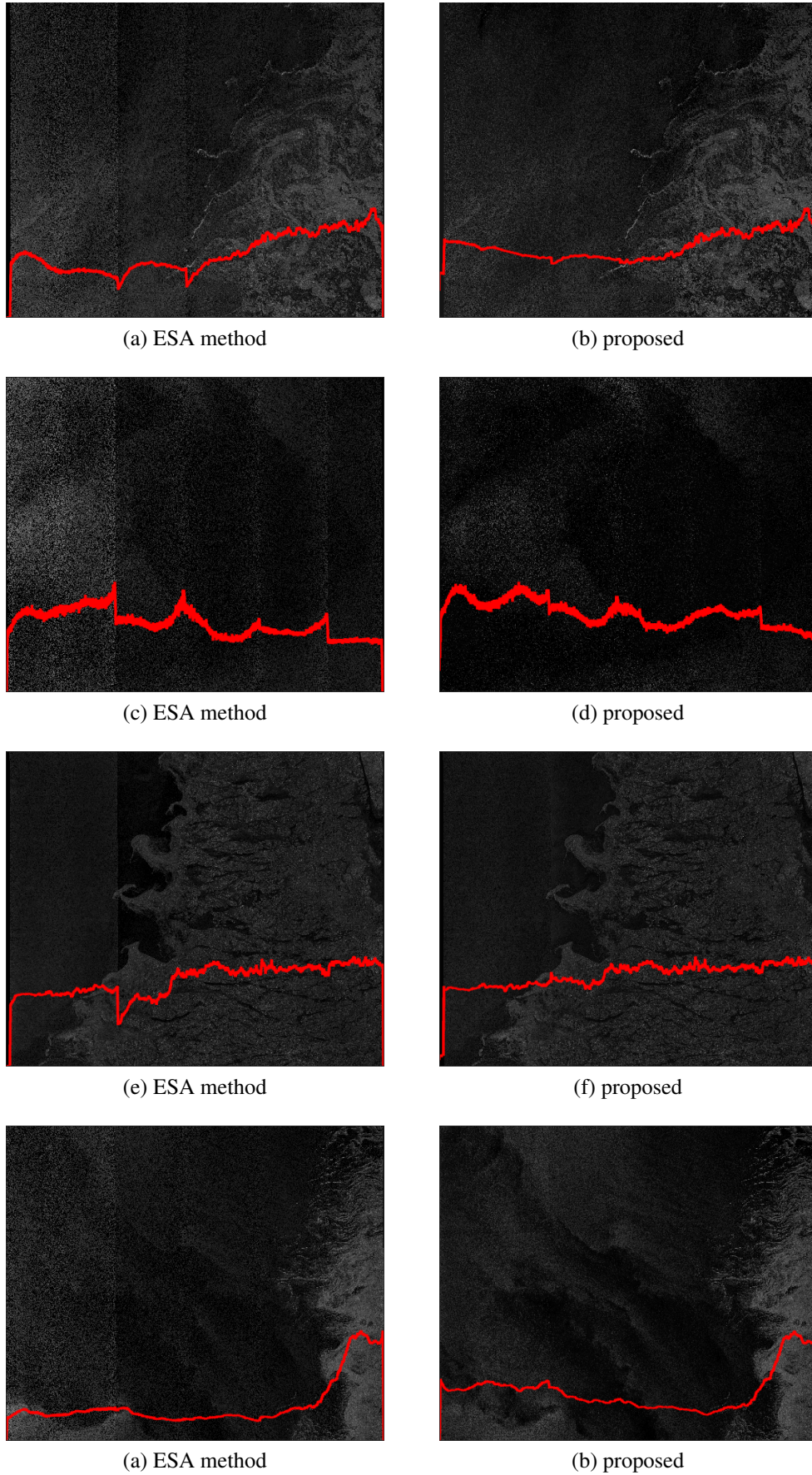


Fig. 6.8 Comparative results obtained with the method described in [24] called ESA method and the proposed one. The mean range profiles overlay the results.

# Chapter 7

## Conclusions

### 7.2 Original contributions

In the following, the main original contributions of the thesis are listed:

- The development of the mathematical formalism for deriving the sparsifying basis associated with the BP algorithm together with the insertion of a nonlinear PSF-based filter for basis vectors selection in the context of the CS greedy solvers [14, 13];
- A SAR focusing procedure, special developed for bistatic sparse multi-aperture acquisition capable to reconstruct missing data using a chirp-based sparsifying dictionary [15, 11];
- A study on various CS solvers was conducted on the bistatic multi-aperture configuration [11];
- A routine for determining the elliptical grid on arbitrary plane for the general bistatic configuration[10];
- A SAR scan-aware focusing workflow for which the polar-elliptical grid special adapted for the factorized BP are directly computed on ground plane [10];
- An novel approach for denoising the cross-polarization Sentinel-1 GRDM images that harnesses the data from the co-polarization channel[12].

## 7.3 List of original publications

### Journals:

1. **A. Focsa**, A. Anghel, M. Datcu and S. -A. Toma, "Mixed Compressive Sensing Back-Projection for SAR Focusing on Geocoded Grid," in IEEE Journal of Selected Topics in Applied Earth Observations and Remote Sensing, vol. 14, pp. 4298-4309, 2021, doi: 10.1109/JSTARS.2021.3072208. (**Impact Factor:3.784 - Q2**)
2. **A. Focsa**, A. Anghel and M. Datcu, "A Compressive-Sensing Approach for Opportunistic Bistatic SAR Imaging Enhancement by Harnessing Sparse Multiaperture Data," in IEEE Transactions on Geoscience and Remote Sensing, vol. 60, pp. 1-14, 2022, Art no. 5205914, doi: 10.1109/TGRS.2021.3071861.(**Impact Factor:5.6 - Q1**)
3. **A. Focsa**, A. Anghel and M. Datcu, "Bistatic planar grid generation for Factorized Back-Projection SAR focusing," in IEEE Geoscience and Remote Sensing Letters (Under review)

### Conference proceedings:

1. Ş. Toma, S. Bogdan, **A. Focşa** and M. Pura, "On Anomalous Deformation Profile Detection Through Supervised and Unsupervised Machine Learning," IGARSS 2019 - 2019 IEEE International Geoscience and Remote Sensing Symposium, 2019, pp. 7419-7422, doi: 10.1109/IGARSS.2019.8898459.
2. **A. Focsa**, S. -A. Toma and D. Gorgoteanu, "On the Interferometric Capabilities of the Pulson P440 UWB Radar," 2021 IEEE International Geoscience and Remote Sensing Symposium IGARSS, 2021, pp. 8201-8204, doi: 10.1109/IGARSS47720.2021.9553329.
3. **A. Focşa**, A. Anghel, Ş. -A. Toma and M. Datcu, "Synthetic Aperture Radar Focusing Based on Back-Projection and Compressive Sensing," IGARSS 2020 - 2020 IEEE International Geoscience and Remote Sensing Symposium, 2020, pp. 2376-2379, doi: 10.1109/IGARSS39084.2020.9323775.
4. **A. Focsa**, M. Datcu, S. -A. Toma, A. Anghel and R. Cacoveanu, "Opportunistic Bistatic SAR Image Classification Using Sub-aperture Decomposition," 2020 13th International Conference on Communications (COMM), 2020, pp. 203-207, doi: 10.1109/COMM48946.2020.9141953.
5. S. -A. Toma, B. Sebacher, D. Teleagă and **A. Focşa**, "Deformation Profile Analysis Using Uniform Manifold Approximation and Projection," IGARSS 2020 - 2020 IEEE International Geoscience and Remote Sensing Symposium, 2020, pp. 4227-4230, doi: 10.1109/IGARSS39084.2020.9323279.
6. **A. Focsa**, M. Datcu and A. Anghel, "Compressed sensing-based multi-aperture focusing of spaceborne transmitter/stationary receiver bistatic SAR data," 2020 IEEE Radar Conference (RadarConf20), 2020, pp. 1-4, doi: 10.1109/RadarConf2043947.2020.9266567.
7. **A. Focşa**, A. Anghel, and M. Datcu, "Inter-polarization Mapping via Gaussian Process Regression for Sentinel-1 EW Denoising," IGARSS 2022 - 2022 IEEE International Geoscience and Remote Sensing Symposium, 2022 (Accepted and presented).

# References

- [1] Alonso, M. T., Lopez-Dekker, P., and Mallorqui, J. J. (2010). A novel strategy for radar imaging based on compressive sensing. *IEEE Transactions on Geoscience and Remote Sensing*, 48(12):4285–4295.
- [2] Anghel, A., Cacoveanu, R., Moldovan, A.-S., Rommen, B., and Datcu, M. (2019). COBIS: Opportunistic C-band bistatic SAR differential interferometry. *IEEE Journal of Selected Topics in Applied Earth Observations and Remote Sensing*, 12(10):3980–3998.
- [3] Blix, K., Espeseth, M. M., and Eltoft, T. (2020). Machine Learning for Arctic Sea Ice Physical Properties Estimation Using Dual-Polarimetric SAR Data. *IEEE Transactions on Geoscience and Remote Sensing*, 59(6):4618–4634.
- [4] Chlailly, S., Kramer, T., Eltoft, T., and Marinoni, A. (2021). A wavelet-based thermal noise removal approach for Sentinel-1 records on polar areas. In *EUSAR 2021; 13th European Conference on Synthetic Aperture Radar*, pages 1–5.
- [5] Cohen, A., Dahmen, W., and DeVore, R. (2017). Orthogonal matching pursuit under the restricted isometry property. *Constructive Approximation*, 45(1):113–127.
- [6] Davidson, M., Gebert, N., and Giulicchi, L. (2021). ROSE-L – The L-band SAR Mission for Copernicus. In *EUSAR 2021; 13th European Conference on Synthetic Aperture Radar*, pages 1–2.
- [7] De Maio, A., Eldar, Y. C., and Haimovich, A. M. (2019). *Compressed sensing in radar signal processing*. Cambridge University Press.
- [8] Dong, X. and Zhang, Y. (2013). A novel compressive sensing algorithm for sar imaging. *IEEE Journal of selected topics in applied earth observations and remote sensing*, 7(2):708–720.
- [9] Dongyang, A., Rui, W., Cheng, H., and Li, Y. (2017). A sparse sar imaging method based on multiple measurement vectors model. *Remote Sensing*, 9(297).
- [10] Focsa, A., Anghel, A., and Datcu, M. (2022a). Bistatic planar grid generation for Factorized Back-Projection SAR focusing. *IEEE Geoscience and Remote Sensing Letters*, –(—):0000–0000.
- [11] Focsa, A., Anghel, A., and Datcu, M. (2022b). A compressive-sensing approach for opportunistic bistatic sar imaging enhancement by harnessing sparse multiaperture data. *IEEE Transactions on Geoscience and Remote Sensing*, 60:1–14.
- [12] Focsa, A., Anghel, A., and Datcu, M. (2022c). Inter-polarization Mapping via Gaussian Process Regression for Sentinel-1 EW Denoising. In *IGARSS 2022 - 2022 IEEE International Geoscience and Remote Sensing Symposium*, pages 0000–0000.

- [13] Focsa, A., Anghel, A., Datcu, M., and Toma, S.-A. (2021). Mixed compressive sensing back-projection for sar focusing on geocoded grid. *IEEE Journal of Selected Topics in Applied Earth Observations and Remote Sensing*, 14:4298–4309.
- [14] Focsa, A., Anghel, A., Toma, S.-A., and Datcu, M. (2020a). Synthetic Aperture Radar Focusing Based on Back-Projection and Compressive Sensing. In *IGARSS 2020 - 2020 IEEE International Geoscience and Remote Sensing Symposium*, pages 2376–2379.
- [15] Focsa, A., Datcu, M., and Anghel, A. (2020b). Compressed sensing-based multi-aperture focusing of spaceborne transmitter/stationary receiver bistatic sar data. In *2020 IEEE Radar Conference (RadarConf20)*, pages 1–4.
- [16] Geudtner, D., Tossaint, M., Davidson, M., and Torres, R. (2021). Copernicus Sentinel-1 Next Generation Mission. In *2021 IEEE International Geoscience and Remote Sensing Symposium IGARSS*, pages 874–876.
- [17] Gorham, L. A. and Moore, L. J. (2010). Sar image formation toolbox for matlab. In *Algorithms for Synthetic Aperture Radar Imagery XVII*, volume 7699, page 769906. International Society for Optics and Photonics.
- [18] Korosov, A., Demchev, D., Miranda, N., Franceschi, N., and Park, J.-W. (2021). Thermal Denoising of Cross-Polarized Sentinel-1 Data in Interferometric and Extra Wide Swath Modes. *IEEE Transactions on Geoscience and Remote Sensing*. (Early Access).
- [19] Lee, P. Q., Xu, L., and Claudi, D. A. (2020). Sentinel-1 additive noise removal from cross-polarization extra-wide TOPSAR with dynamic least-squares. *Remote Sensing of Environment*, 248:111982.
- [20] Lee, P. Q., Xu, L., and Claudi, D. A. (2021). Estimating Noise Floor in Sentinel-1 Images With Linear Programming and Least Squares. *IEEE Transactions on Geoscience and Remote Sensing*, pages 1–14.
- [21] M. Bourbigot, H. Johnsen, R. Piantanida, G. Hajduch, and J. Poullaouec (2016). Sentinel-1 Product Definition. Technical Report S1-RS-MDA-52-7440, Collecte Localisation Satellites (CLS).
- [22] Park, J.-W., Won, J.-S., Korosov, A. A., Babiker, M., and Miranda, N. (2019). Textural noise correction for Sentinel-1 TOPSAR cross-polarization channel images. *IEEE Transactions on Geoscience and Remote Sensing*, 57(6):4040–4049.
- [23] Piantanida, R., Hajduch, G., and Poullaouec, J. (2016). Sentinel-1 level 1 detailed algorithm definition. *ESA, techreport SEN-TN-52-7445*.
- [24] Piantanida, R., Miranda, N., and Hadjduch, G. (2017). Thermal Denoising of Products Generated by the S-1 IPF. *Sentinel-1 Mission Perform. Centre, Ramonville-Saint-Agne, France, Tech. Rep. MPC-0392*.
- [25] Rasmussen, C. E. (2003). Gaussian processes in machine learning. In *Summer school on machine learning*, pages 63–71. Springer.
- [26] Rodriguez-Cassola, M., Prats-Iraola, P., Krieger, G., and Moreira, A. (2019). On the use of time-domain SAR focusing in spaceborne SAR missions. In *IGARSS 2019-2019 IEEE International Geoscience and Remote Sensing Symposium*, pages 755–758. IEEE.

- [27] Soumekh, M. (1999). *Synthetic aperture radar signal processing*, volume 7. New York: Wiley.
- [28] Sun, Y. and Li, X.-M. (2021). Denoising Sentinel-1 Extra-Wide Mode Cross-Polarization Images Over Sea Ice. *IEEE Trans. Geosci. Remote. Sens.*, 59(3):2116–2131.
- [29] Ulander, L. M., Hellsten, H., and Stenstrom, G. (2003). Synthetic-aperture radar processing using fast factorized back-projection. *IEEE Transactions on Aerospace and electronic systems*, 39(3):760–776.
- [30] Yegulalp, A. F. (1999). Fast backprojection algorithm for synthetic aperture radar. In *Proceedings of the 1999 IEEE Radar Conference. Radar into the Next Millennium (Cat. No. 99CH36249)*, pages 60–65. IEEE.